RESEARCH ARTICLE

The **FASEB** Journal

Invasive electrochemical impedance spectroscopy with phase delay for experimental atherosclerosis phenotyping

Michael Chen[1] | **Natalia Neverova**[1,2,3] | **Shili Xu**[4,5] | **Krit Suwannaphoom**[6] | **Gentian Lluri**[1,2] | **Mikayla Tamboline**[4] | **Sandra Duarte**[7] | **Michael C. Fishbein**[6] | **Yuan Luo**[8] | **René R. Sevag Packard**[1,2,3,5,9,10,11,12]

[1]Division of Cardiology, Department of Medicine, David Geffen School of Medicine, University of California, Los Angeles, California, USA

[2]Ronald Reagan UCLA Medical Center, Los Angeles, California, USA

[3]West Los Angeles Veterans Affairs Medical Center, Los Angeles, California, USA

[4]Crump Institute for Molecular Imaging, Department of Molecular and Medical Pharmacology, David Geffen School of Medicine, University of California, Los Angeles, California, USA

[5]Jonsson Comprehensive Cancer Center, University of California, Los Angeles, California, USA

[6]Department of Pathology and Laboratory Medicine, David Geffen School of Medicine, University of California, Los Angeles, California, USA

[7]Division of Laboratory and Animal Medicine, University of California, Los Angeles, California, USA

[8]State Key Laboratory of Transducer Technology, Shanghai Institute of Microsystem and Information Technology, Chinese Academy of Sciences, Shanghai, People's Republic of China

[9]Department of Physiology, David Geffen School of Medicine, University of California, Los Angeles, California, USA

[10]Department of Bioengineering, Henry Samueli School of Engineering and Applied Science, University of California, Los Angeles, California, USA

[11]Molecular Biology Institute, University of California, Los Angeles, California, USA

[12]California NanoSystems Institute, University of California, Los Angeles, California, USA

Correspondence
René R. Sevag Packard, Division of Cardiology, Department of Medicine, UCLA, 10833 Le Conte Ave., CHS Building Room 43-268, Los Angeles, CA 90095, USA.
Email: rpackard@mednet.ucla.edu

Abstract

Distinguishing quiescent from rupture-prone atherosclerotic lesions has significant translational and clinical implications. Electrochemical impedance spectroscopy (EIS) characterizes biological tissues by assessing impedance and phase delay responses to alternating current at multiple frequencies. We evaluated invasive 6-point stretchable EIS sensors over a spectrum of experimental atherosclerosis and compared results with intravascular ultrasound (IVUS), molecular positron emission tomography (PET) imaging, and histology. Male New Zealand White rabbits ($n = 16$) were placed on a high-fat diet, with or without endothelial denudation via balloon injury of the infrarenal abdominal aorta. Rabbits underwent in vivo micro-PET imaging of the abdominal aorta with ^{68}Ga-DOTATATE,

Abbreviations: AC, alternating current; ACS, acute coronary syndrome; BSC, background subtraction correction; CAD, coronary artery disease; CRP, C-reactive protein; CT, computed tomography; CTA, computed tomography angiography; EIS, electrochemical impedance spectroscopy; FFR, fractional flow reserve; FFR-CT, fractional flow reserve by computed tomography; ^{18}F-FDG, ^{18}F-fluorodeoxyglucose; ^{18}F-NaF, ^{18}F-sodium fluoride; ^{68}Ga-DOTATATE, ^{68}Ga-tetraazacyclododecanetetraacetic acid-DPhe1-Tyr3-octreotate; HDL, high-density lipoprotein; %ID/cc, % injected dose per cubic centimeter; IVUS, intravascular ultrasound; LDL, low-density lipoprotein; NIRF, near-infrared fluorescence; NZW, New Zealand White; OCT, optical coherence tomography; PBS, phosphate-buffered saline; PET, positron emission tomography; ROI, region of interest; SMC, smooth muscle cell; SSTR2, somatostatin receptor 2; TBR, target-to-background ratio.

UC | University of California, Los Angeles (UCLA)

^{18}F-NaF, and ^{18}F-FDG, followed by invasive interrogation via IVUS and EIS. Background signal-corrected values of impedance and phase delay were determined. Abdominal aortic samples were collected for histology. Analyses were performed blindly. EIS impedance was associated with markers of plaque activity including macrophage infiltration ($r = .813$, $p = .008$) and macrophage/smooth muscle cell (SMC) ratio ($r = .813$, $p = .026$). Moreover, EIS phase delay correlated with anatomic markers of plaque burden, namely intima/media ratio ($r = .883$, $p = .004$) and %stenosis ($r = .901$, $p = .002$), similar to IVUS. ^{68}Ga-DOTATATE correlated with intimal macrophage infiltration ($r = .861$, $p = .003$) and macrophage/SMC ratio ($r = .831$, $p = .021$), ^{18}F-NaF with SMC infiltration ($r = -.842$, $p = .018$), and ^{18}F-FDG correlated with macrophage/SMC ratio ($r = .787$, $p = .036$). EIS with phase delay integrates key atherosclerosis features that otherwise require multiple complementary invasive and non-invasive imaging approaches to capture. These findings indicate the potential of invasive EIS to comprehensively evaluate human coronary artery disease.

KEYWORDS

atherosclerosis, electrochemical impedance spectroscopy, intravascular ultrasound, positron emission tomography, rabbit

1 | INTRODUCTION

Cardiovascular disease remains the leading cause of mortality in the United States, accounting for 20.1% of all deaths, often due to coronary artery disease (CAD) complications.[1] We have significantly progressed in our understanding of the pathobiology of atherosclerosis. In particular, lesional macrophage infiltration, neo-intimal macrophage-to-vascular smooth muscle cell (SMC) ratio, presence of a necrotic core overlain by a thin fibrous cap, positive remodeling, and spotty calcification, among others, are now appreciated as indicators of rupture-prone, inflammatorily active, "vulnerable" plaques.[2] In contemporary clinical practice promoting aggressive lipid-lowering strategies, we have furthermore witnessed an increase in the incidence of endothelial erosion as opposed to fibrous cap rupture as the underlying mechanism leading to acute coronary syndromes (ACS).[3] Accordingly, there is significant translational and clinical interest in the development of invasive and non-invasive imaging strategies to reveal pertinent components of atherosclerotic lesions prior to downstream clinical events.

Non-invasive imaging modalities such as coronary computed tomography angiography (CTA) provide comprehensive visualization of the entire coronary tree and the severity, type, calcification, and extent of atherosclerotic plaques, an assessment that can be augmented by fractional flow reserve by computed tomography (FFR-CT).[4] Positron emission tomography (PET) evaluation of the coronary arteries, beyond myocardial perfusion imaging and myocardial blood flow quantitation,[5] can provide information on specific plaque components such as macrophage infiltration via ^{68}Ga-tetraazacyclo dodecanetetraacetic acid-DPhe1-Tyr3-octreotate (^{68}Ga-DOTATATE),[6] microcalcification via ^{18}F-sodium fluoride (^{18}F-NaF),[7] and metabolic/inflammatory activity via ^{18}F-fluorodeoxyglucose (^{18}F-FDG).[8] However, non-invasive imaging modalities suffer from drawbacks, such as blooming artifacts and need for contrast agents in coronary CTA, and the limited spatial resolution and reliance on radiotracers for PET imaging.[9]

Invasive imaging modalities can help guide CAD management by directly characterizing target atherosclerotic lesions. Intravascular ultrasound (IVUS) is a well-established, catheter-based imaging method capable of measuring vessel wall dimensions, determining plaque phenotype such as degree of atherosclerosis burden and calcification, and assessing the distribution and severity of plaques along a vessel. However, IVUS cannot accurately discriminate among plaque components and has relatively lower spatial resolution compared to other invasive imaging modalities.[10] Optical coherence tomography (OCT) complements the strengths and limitations of IVUS. OCT utilizes near-infrared light to generate cross-sectional images of a sample by calculating the delay times between different light rays detected by

the sensor, and boasts a 10-fold higher spatial resolution than IVUS, although at the expense of a lower penetration depth.[11,12] Near-infrared fluorescence (NIRF) also utilizes near-infrared light, which, instead of directly interrogating the sample, stimulates fluorophores that localize and interact with the target of interest. NIRF provides deep tissue penetration, mainly due to low signal attenuation from blood and lower background noise from tissue autofluorescence, and is capable of assessing plaque inflammation in vivo.[13]

Ideally, invasive coronary imaging should elucidate the structural and compositional features of the interrogated atherosclerotic lesion. Electrochemical impedance spectroscopy (EIS) assesses the resistive and charge-storing characteristics of biological tissue by measuring the impedance that develops in response to an applied alternating current (AC). By interrogating a sample over a range of AC frequencies, the frequency-dependent electrical properties of a tissue sample, such as impedance, a measure of resistance to current flow, can be determined.[14] Our group previously demonstrated that EIS distinguishes lipid-laden atherosclerotic lesions from healthy arterial segments.[15,16] Further improvements to the initial linear two-point sensor yielded a 6-point circumferential design capable of 360° interrogation of the endoluminal surface, thus accounting for the eccentric nature of atherosclerosis.[16] In the present study, we incorporated background signal correction for impedance, integrated the EIS phase delay, (i.e., the offset between input and output signals), and determined the diagnostic performance of invasive EIS over a wide spectrum of atherosclerosis disease severity conditions in a New Zealand White (NZW) rabbit model. We further interrogated resultant plaque phenotypes via ⁶⁸Ga-DOTATATE, ¹⁸F-NaF, and ¹⁸F-FDG micro-PET/CT imaging and by IVUS, and conducted histological analyses of pertinent plaque parameters. Our results establish invasive EIS with phase delay as a strategy providing complementary phenotypic and structural atherosclerotic plaque characterization, thereby permitting the distinction between apparently stable and more advanced lesions.

2 | METHODS

2.1 | Animals

Male NZW rabbits ($n = 16$), ages 12–16 weeks and weighing 3–3.5 kg upon arrival (Crl:KBL, Charles River, Wilmington, MA, USA), were fed a 5% peanut oil and 1% cholesterol high-fat diet (LabDiet, Arden Hills, MN, USA) for either 4 ($n = 8$) or 8 ($n = 8$) weeks (Figure S1).

Endothelial denudation via balloon injury was also performed in $n = 8$ rabbits prior to the initiation of the high-fat diet to create a spectrum of atherosclerotic lesions. All institutional and national guidelines for the care and use of laboratory animals were followed and approved by the UCLA Office of Animal Research.

2.2 | EIS sensor microfabrication

The 6-point EIS sensor was fabricated in-house as previously described.[16] Briefly, flexible polyimide strips (FPCexpress, Concord, ON, Canada) with exposed copper pads (600 μm x 300 μm) serving as the electrodes were mounted onto an inflatable balloon (Poba Medical, Flagstaff, AZ, USA) (15 mm in length, <1 mm diameter under deflation, and ~4.5 mm under inflation), which was affixed onto the distal end of the catheter tubing (25 cm in length) (Nordson Medical, Salem, NH, USA). Tantalum foils (1 mm × 1 mm) (Advent Research Materials, Eynsham, Oxfordshire, UK) were placed immediately distal and proximal to the balloon to serve as radiopaque markers. Insulated copper wires were soldered onto the proximal contact pads of the flexible sensors to be connected to an impedance analyzer (Interface 1010E, Gamry Instruments, Warminster, PA, USA). Electroplating was performed in a solution of 0.5% w/v $PtCl_4$ at −0.6 V for 30 min to minimize contact impedance and improve EIS measurement specificity.

2.3 | Blood work

Blood samples for total cholesterol, low- (LDL), and high- (HDL) density lipoprotein cholesterol, triglycerides, and C-reactive protein (CRP) (VRL Diagnostics, San Antonio, TX, USA) were collected prior to high-fat diet initiation and 24 h prior to harvesting following overnight fast.

2.4 | Balloon injury

General anesthesia was induced via intravenous administration of ketamine (10 mg/kg) and dexmedetomidine (10 mcg/kg). Rabbits were placed on a mechanical ventilator via endotracheal intubation to deliver isoflurane (2–3.5%) for maintenance of anesthesia throughout the duration of the procedure. A cutdown was performed in the right inguinal area to expose the right femoral artery. A 5-French vascular sheath (Terumo, Somerset, NJ, USA) was inserted into the right femoral artery and a 3-French thru-lumen embolectomy balloon catheter (Edwards

Lifesciences, Irvine, CA, USA) was advanced under fluoroscopic guidance (Siemens Artis Zeego with robotic arm) and iodine contrast (Ultravist 300 mg/mL, McKesson, Irving, TX, USA) injection through the abdominal aorta to 2 cm caudal from the takeoff of the left renal artery (Figure S2). The balloon catheter was inflated, and three back-and-forth pullbacks over a 2 cm region were performed. The sheath was removed, femoral artery ligated, and surgical site closed in layers with absorbable sutures. Following closure of incised skin, meloxicam (oral, 0.02 mg/kg, once every 24 h for 48 h) and buprenorphine (subcutaneous, 0.5 mg/kg, every 12 h for 48 h) were administered for pain relief.

2.5 | Micro-PET/CT imaging

All animals were imaged 72 h (^{68}Ga-DOTATATE), 48 h (^{18}F-NaF), and 24 h (^{18}F-FDG) prior to harvesting. Animals were fasted overnight prior to ^{18}F-FDG imaging. Animals were injected with either 37 MBq (^{68}Ga-DOTATATE, ^{18}F-NaF) or 111 MBq (^{18}F-FDG) of radiotracer diluted in 0.5–1 mL sterile saline solution (0.9% w/v NaCl) via the marginal ear vein. After injection, 1 h, 1.5 h, or 3 h was allowed for uptake of ^{68}Ga-DOTATATE, ^{18}F-NaF, or ^{18}F-FDG, respectively. Following the uptake period, animals were anesthetized using the aforementioned procedure and maintained on anesthesia using isoflurane delivered through a nose cone, placed prone on the scanner bed, and positioned such that the scanner field of view (12 cm width) was centered 2 cm caudal to the left renal takeoff. Micro-PET (350–650 keV, 7-minute scan time, 0.5435 mm voxel size) and low-attenuation CT (80kVp, 150 μA, 720 projections, 1-minute scan time) images were acquired on a GNEXT micro-PET/CT scanner (Sofie Biosciences, Dulles, VA, USA). After micro-PET/CT image acquisition, 5 mL of Ultravist 300 was injected via the marginal ear vein, and contrast CT image acquisition was initiated. An additional 5 mL of Ultravist 300 followed by 5 mL sterile saline and 1 mL 0.1% heparin flush were injected over the first 30 seconds of the contrast CT scan. All fluids were kept on a heating pad prior to injection. The total contrast CT scan time was 90 seconds. Micro-PET/CT and contrast CT scans were repeated for the chest area using the aforementioned procedures.

Micro-PET images were reconstructed using a 3D-ordered subset expectation maximization (OSEM) algorithm (24 subsets and 3 iterations), with random, attenuation, and decay correction. The CT images were reconstructed using a modified Feldkamp algorithm. PET and CT images were interpolated using trilinear interpolation (AMIDE). The low-attenuation CT and contrast CT images were aligned using bone structures as reference. Once the datasets were aligned, a cylindrical region of interest (ROI) of 3 mm radius and 20 mm length was placed on the abdominal aorta 2–4 cm caudal to the left renal takeoff. To correct for background blood pool activity in PET images, a spherical ROI with radius of 2 mm was placed in the right atrium. The %ID/cc values were obtained for PET data quantification and analysis.

2.6 | IVUS

Prior to EIS measurements, an IVUS catheter (Makoto Intravascular Imaging System, Infraredx, Bedford, MA, USA) was advanced through the sheath under fluoroscopic guidance to 2 cm caudal to the left renal artery takeoff. A 2 cm region was interrogated using a pullback speed of 0.5 mm/s. IVUS images were analyzed for plaque burden, defined as $\frac{E-L}{E}$, where E is the area enclosed by the external elastic membrane and L is the area of the lumen.

2.7 | EIS measurements

EIS was performed in vivo, under general anesthesia using the aforementioned procedures, and immediately prior to animal euthanasia. Following placement of a 5-French sheath via femoral artery, an EIS sensor catheter was inserted and advanced into the abdominal aorta under fluoroscopic guidance to 2–4 cm caudal of the left renal artery takeoff (Figure S2A). The balloon was inflated until contact was made with the endoluminal surface. Two replicates of all 15 pairwise permutations of EIS measurements were obtained from 1 Hz to 1 MHz using AC signals with peak-to-peak voltages of 50 mV and 5 data points per decade (Figure S2B). Impedance (Ω) and phase delay (°) were quantified. Prior to inflating the balloon, a set of measurements were also obtained with the balloon deflated to verify specificity of EIS signals.

Analysis of EIS measurements was performed within the subrange of 40 Hz–40 kHz given that this constitutes the "plateau region" over which impedance values are stable, thus permitting accurate comparisons between measurements.[15] The diagnostic performance of impedance and phase delay raw values, target-to-background ratios (TBR: inflated ÷ deflated), and background subtraction correction (BSC: inflated − deflated) was determined. Within the 15 pairwise measurements constituting one full set of EIS measurements, the

maximum impedance TBR and minimum (i.e., most negative) phase delay BSC outperformed the other metrics. Accordingly, reported impedance and phase delay values represent the max TBR and minimum BSC values, respectively. Separately, ex vivo EIS measurements of abdominal aortas from a control rabbit (not fed a high-fat diet) and an experimental rabbit were performed with all catheters that were utilized for the in vivo EIS measurements to assess the stability of EIS measurements across different catheter units.

2.8 | Histology

The region of the abdominal aorta 2–4 cm caudal to the left renal artery takeoff was collected following IVUS and EIS interrogation. Tissues were washed in phosphate-buffered saline (PBS), fixed in 10% formalin, and stored in 70% ethanol. Samples were then embedded in paraffin, sectioned, and stained with hematoxylin and eosin and Masson's trichrome (Statlab, McKinney, TX, USA) staining methods. Immunohistochemistry was performed to detect vascular SMCs (α-actin, Agilent Dako, Santa Clara, CA, USA). Atherosclerotic plaques were analyzed for intima/media thickness ratio, %stenosis, macrophage infiltration, SMC infiltration, and macrophage/SMC ratio. %Stenosis was defined as the ratio of the endoluminal surface circumference to the internal elastic lamina circumference. The thicknesses of the intimal and medial layers were measured at four locations equidistant from each other along the internal and external elastic laminas. The intima/media thickness ratio was calculated by dividing the maximum intimal thickness by the maximum medial thickness. %SMC infiltration was obtained by calculating the percent intimal area that displayed positive α-actin staining. Macrophage infiltration was evaluated visually by experienced pathologists (K.S. and M.C.F). All analyses were conducted blinded. Arteries that displayed the early stages of atherosclerotic plaque formation, namely focal neointima with minimal macrophage infiltration, extracellular matrix, and neointimal SMCs, were categorized as "plaque initiation." Arteries with "plaque progression" exhibited neointimal thickening and increased macrophage accumulation, extracellular matrix, and neointimal SMCs.

2.9 | Statistics

Results are presented as mean ± standard error or Pearson correlations. Two-tailed paired Student's t-tests were performed to assess differences in serum biomarker levels. One-way ANOVA with post hoc Tukey's test was performed to evaluate consistency of EIS measurements among the different catheters utilized. The Shapiro–Wilk test was performed to assess normality of datasets. The Pearson correlation coefficient was used for comparison of IVUS-derived plaque burden, micro-PET/CT results, impedance, and phase delay against histological parameters. Stata v17 (StataCorp., College Station, TX, USA), SPSS v26 (IBM, Armonk, NY, USA), and Prism version 9 (GraphPad, Boston, MA, CA) were used for statistical analyses. A p-value $<.05$ was considered significant.

3 | RESULTS

3.1 | Blood work

Serum lipid levels (total-, LDL-, and HDL-cholesterol, and triglycerides) and C-reactive protein (CRP) were low in all animals at baseline and significantly increased at time of harvest, indicating presence of proatherogenic conditions (Figure S3).

3.2 | Histology

Representative examples from infrarenal abdominal aortas with absent, initiating, and progressing plaques are presented in Figure S4. The bimodal distributions of atherosclerotic plaque characteristics, namely intima/media ratio (Figure S5A), macrophage infiltration (Figure S5B), SMC infiltration (Figure S5C), and macrophage/SMC ratio (Figure S5D), reflect histological differences between initiating and progressing plaques.

3.3 | Micro-PET/CT

Rabbits underwent in vivo micro-PET/CT imaging on consecutive days to evaluate macrophage presence by ^{68}Ga-DOTATATE, microcalcification by ^{18}F-NaF, and metabolic activity by ^{18}F-FDG, respectively, within the infrarenal abdominal aortic region of interest (Figure 1A–C, Figure S6). The mean % injected dose per cubic centimeter (%ID/cc) of ^{68}Ga-DOTATATE strongly correlated with intimal macrophage infiltration ($r=.861$, $p=.003$) and macrophage/SMC ratio ($r=.831$, $p=.021$) (Figure 1D,E). Mean %ID/cc TBR of ^{18}F-FDG moderately correlated with macrophage/SMC ratio ($r=.787$, $p=.036$) but not

with macrophage infiltration alone ($r=.524$, $p=.147$) (Figure 1F,G), intima/media ratio ($r=-.311$, $p=.415$), or %stenosis ($r=-.284$, $p=.458$). Mean %ID/cc TBR of ^{18}F-NaF strongly correlated with SMC infiltration ($r=-.842$, $p=.018$) (Figure S6).

3.4 | IVUS

Plaque burden determined by IVUS correlated significantly with both intima/media ratio ($r=.939$, $p<.001$) and %stenosis ($r=.892$, $p=.001$) (Figure 2).
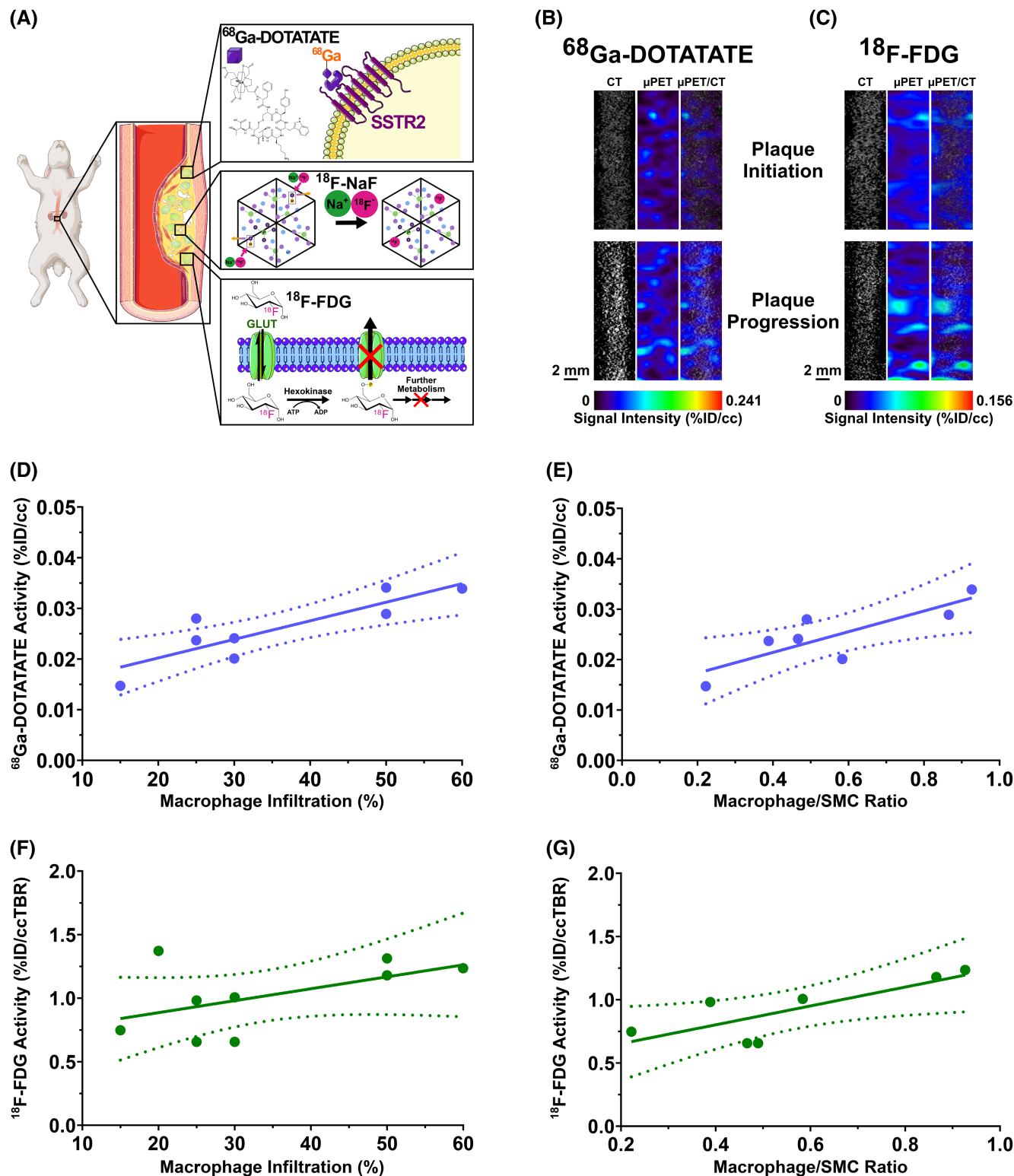
FIGURE 1 Detection of atherosclerotic components by PET radiotracers. (A) Schematic representing the molecular mechanisms of ^{68}Ga-DOTATATE (top), ^{18}F-NaF (middle), and ^{18}F-FDG (bottom) imaging. (B and C) Representative 2D projections of images of the infrarenal abdominal aorta region of interest obtained via CT (left columns), µPET (middle columns), and combined µPET/CT (right columns) with (B) ^{68}Ga-DOTATATE and (C) ^{18}F-FDG obtained on consecutive days to evaluate macrophage presence and metabolic activity. Arteries that displayed the early stages of atherosclerotic plaque formation, namely focal neointima with minimal macrophage infiltration, extracellular matrix, and neointimal SMCs, were categorized as "plaque initiation." Arteries with "plaque progression" exhibited neointimal thickening and increased macrophage accumulation, extracellular matrix, and neointimal SMCs. Activities of ^{68}Ga-DOTATATE and ^{18}F-FDG both correlated with histological plaque parameters of interest. (D and E) Mean %ID/cc of ^{68}Ga-DOTATATE strongly correlated with intimal macrophage infiltration ($r = .861$, $p = .003$) and macrophage/SMC ratio ($r = .831$, $p = .021$). (F and G) Mean ^{18}F-FDG %ID/cc TBR trended toward correlation with macrophage infiltration ($r = .524$, $p = .147$) without statistical significance, but did moderately correlate with macrophage/SMC ratio ($r = .787$, $p = .036$). Pearson correlation coefficients were calculated for comparison of PET radiotracer activity against histological parameters. For each radiotracer, all CT images and all PET images were obtained using the same scale. %ID/cc, % injected dose per cubic centimeter; ^{18}F-FDG, ^{18}F-fluorodeoxyglucose; ^{68}Ga-DOTATATE, ^{68}Ga-tetraazacyclododecanetetraacetic acid-DPhe1-Tyr3-octreotate; CT, computed tomography; PET, positron emission tomography; SMC, smooth muscle cell; SSTR2, somatostatin receptor 2; TBR, target-to-background ratio.
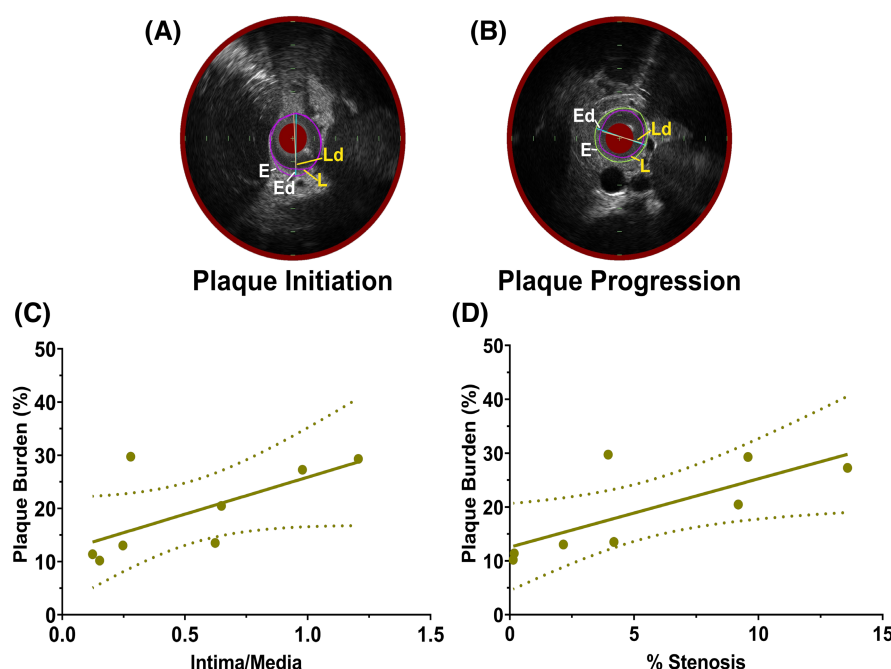

FIGURE 2 Plaque burden quantitation by IVUS. (A and B) Representative IVUS images. Plaque burden, defined as $\frac{E-L}{E}$, was calculated from IVUS images by comparing the areas enclosed by the external elastic lamina, E, and the lumen, L. Ed and Ld represent the maximum diameters of the areas enclosed by the external elastic lamina and the lumen, respectively. Examples from an early atherosclerotic lesion (plaque initiation) (A) and a more developed lesion (plaque progression) (B). Plaque burden correlated significantly with both (C) intima/media ratio ($r = .939$, $p < .001$) and (D) %stenosis ($r = .892$, $p = .001$). Pearson correlation coefficients were calculated for comparison of IVUS-derived plaque burden against histological parameters. IVUS, intravascular ultrasound.

3.5 | EIS impedance and phase delay

3.5.1 | Determination of stable impedance "plateau region" for EIS data analysis

Whereas biological systems demonstrate both capacitive and resistive behavior, the lower and higher impedance frequency regimes are dominated by either capacitive or resistive behavior, respectively, and thus do not provide reliable measurements. Accordingly, analyses of EIS measurements were performed with data from 40 Hz to 40 kHz, the "plateau region". Within this frequency range, impedance signals are stable, thus allowing for accurate comparisons between measurements and conditions (Figures 3 and 4).
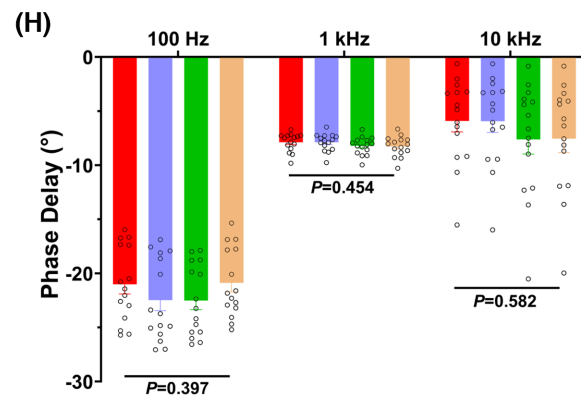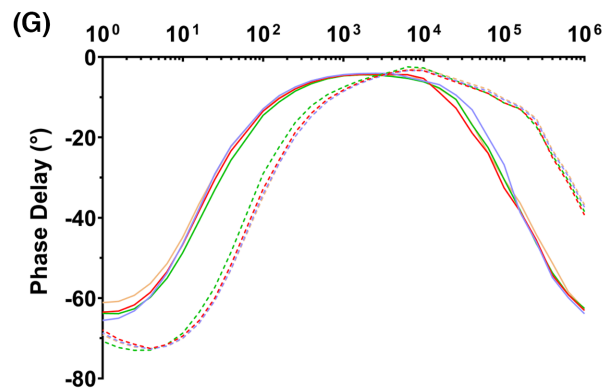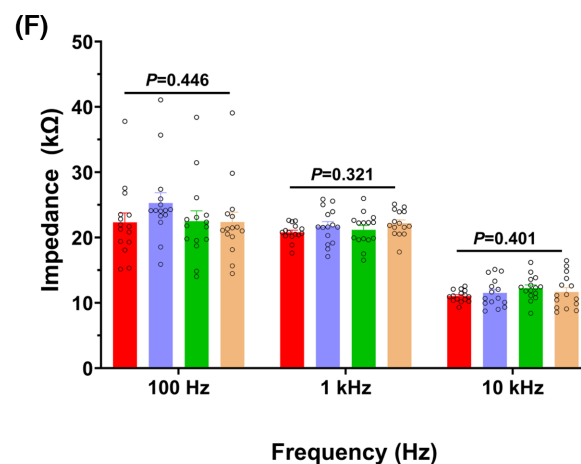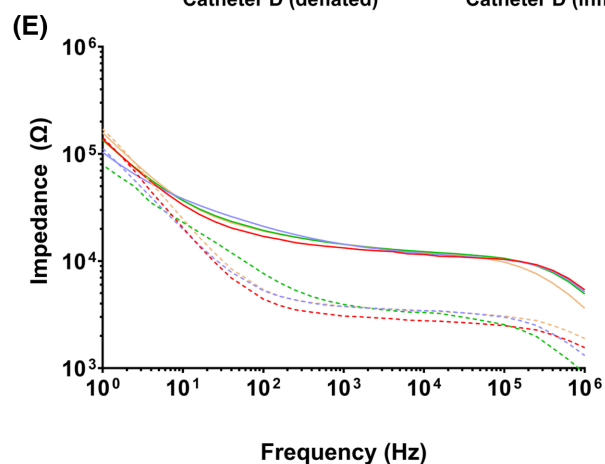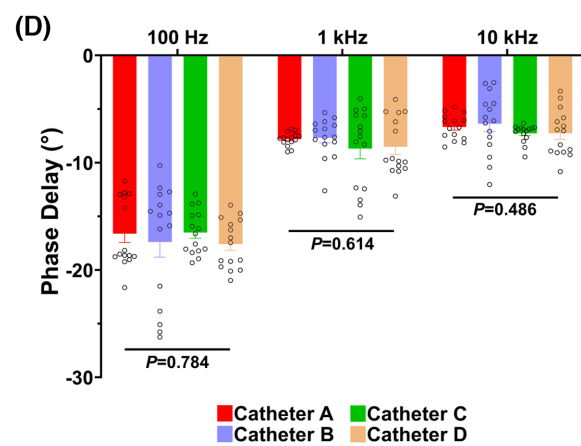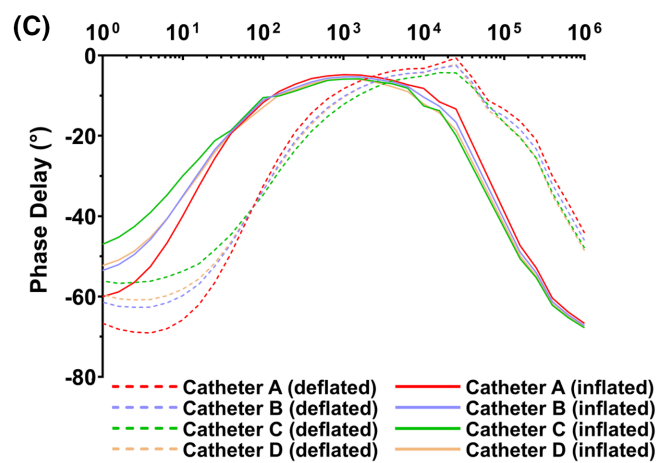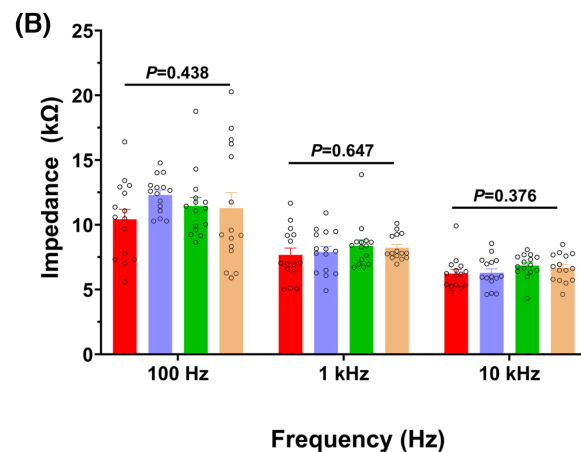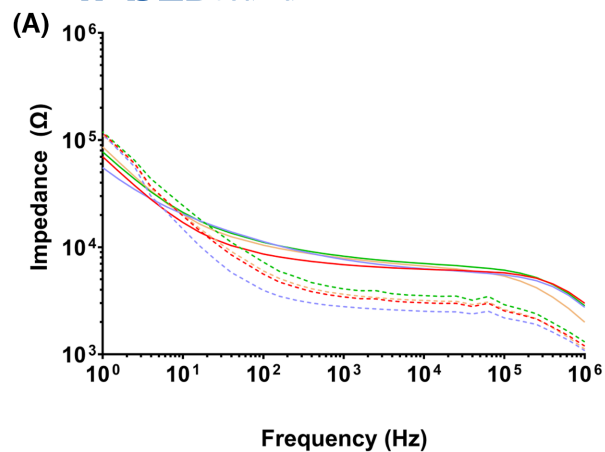
FIGURE 3 Ex vivo assessment of EIS measurement stability among multiple catheters. The stability of (A and B, E and F) impedance and (C and D, G and H) phase delay measurements between the different catheters utilized for in vivo interrogation was assessed by separately measuring the ex vivo impedance and phase delay profiles of abdominal aorta segments from a (A–D) control (not fed a high-fat diet) and an (E–H) experimental (fed a high-fat diet) rabbit in 70 mM NaCl solution. (A, C, E, and G) Measurements were performed with the sensor balloon inflated (solid lines) and deflated (dashed lines). Each color represents a different EIS catheter used for in vivo measurements, which are named to distinguish one from another but are otherwise identical. (B, D, F, and H) One-way ANOVA with post hoc Tukey's test was performed at three frequencies from the "plateau region": 100 Hz, 1 kHz, and 10 kHz. Neither the impedance nor the phase delay displayed significant differences among all catheters at all frequencies tested. EIS, electrochemical impedance spectroscopy.

3.5.2 | EIS demonstrates signal specificity between inflated and deflated measurements

There were marked differences in impedance and phase delay under balloon inflation versus deflation, reflecting changes in endoluminal microsensor contact (Figures 3A,C,E,G and 4A–D). Following impedance TBR measurement, max TBR—selected from $n = 15$ individual values to capture potential heterogeneities in eccentric atherosclerotic lesions—was superior to max background subtraction correction (BSC) and uncorrected ("raw") max impedance in the number and strength of correlations with histological plaque features. For phase delay, the minimal (i.e., most negative) BSC—also selected from $n = 15$ individual values—performed better than TBR and uncorrected phase delay.

3.5.3 | EIS measurements are reproducible across different catheters

The performance of all the catheters utilized for in vivo EIS measurements (labeled Catheters A to D) was assessed separately ex vivo under control (Figure 3A–D) and high-fat conditions (Figure 3E–H). Interrogation of the abdominal aorta in a control rabbit (i.e., not fed a high-fat diet) over a range of frequencies within the "plateau region" indicated similar impedance results at 100 Hz ($p = .438$), 1 kHz ($p = .647$), and 10 kHz ($p = .376$) (Figure 3B), as well as similar phase delay results (100 Hz: $p = .784$; 1 kHz: $p = .614$; 10 kHz: $p = .486$) (Figure 3D). This was also the case for an abdominal aorta from an experimental rabbit fed a high-fat diet, for which neither impedance (100 Hz: $p = .446$; 1 kHz: $p = .321$; 10 kHz: $p = .401$) (Figure 3F) nor phase delay (100 Hz: $p = .397$; 1 kHz: $p = .454$; 10 kHz: $p = .582$) (Figure 3H) displayed significant differences among the various catheters.

3.5.4 | Impedance and phase delay characterize atherosclerosis composition and morphology

The EIS stretchable microelectrodes were affixed on an inflatable balloon, permitting capture of impedance and phase delay results under inflated and deflated conditions and derivation of TBR. In addition, the two rings of three microelectrodes permit 360° interrogation of the arterial segment of interest in vertical, oblique, and horizontal axes, for a total of $n = 15$ pairwise permutations (Figure S2B).

Invasive EIS metrics were evaluated in vivo for detection of atherosclerotic compositional and structural features. There were distinct impedance and phase delay profiles in initiating versus progressing atherosclerotic lesions (Figure 4). Impedance profiles of the "plateau region" demonstrated an upward shift leading to higher impedance in more developed plaques compared to early plaques (16.9 kΩ vs. 10.3 kΩ, $p < .001$) (Figure 4A,C,E). Whereas phase delay of early plaques peaked at higher frequencies (5 kHz—15 kHz), more developed lesions exhibited a leftward shift of phase delay profile leading to a peak phase delay at lower frequencies (0.1 kHz—1 kHz) (Figure 4B,D,F).

In addition, impedance TBR detected compositional plaque features and exhibited significant correlation with macrophage infiltration ($r = .813$, $p = .008$) (Figure 5A) and macrophage/SMC ratio ($r = .813$, $p = .026$) (Figure 5B). Lesions with higher inflammatory burden exhibited an increase in impedance values. Furthermore, phase BSC demonstrated significant correlation with structural plaque characteristics, namely intima/media ratio ($r = .883$, $p = .004$) (Figure 5C) and with %stenosis ($r = .901$, $p = .002$) (Figure 5D). Thus, whereas impedance detects key compositional features, EIS phase delay captures pertinent atherosclerotic morphological features (Figure 6).

4 | DISCUSSION

A modality capable of robustly characterizing atherosclerosis features associated with downstream complications might prove a powerful strategy leading to potential changes in therapy. In the present body of work, we demonstrate the capability of 3-D EIS to serve as a comprehensive modality for atherosclerosis characterization by (i) unraveling histological markers of high-risk lesions including macrophage infiltration and macrophage/vascular SMC ratio, via impedance sweep, and (ii) determining atherosclerosis structural features including %stenosis and intima/media ratio, via phase delay. We further
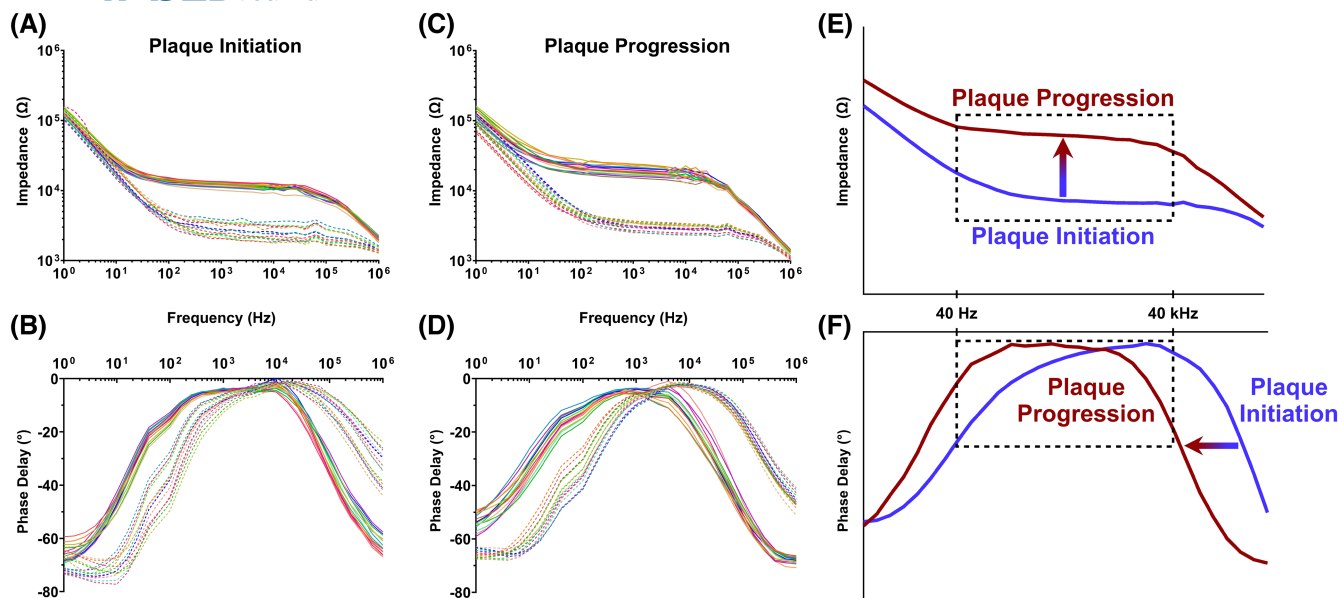
FIGURE 4 In vivo EIS impedance and phase delay profiles vary with lesion progression. Representative (A and C) impedance and (B and D) phase delay profiles of in vivo EIS measurements of rabbit abdominal aortas are presented. Measurements were performed with the sensor balloon inflated (solid lines) and deflated (dashed lines). Each color represents a different EIS sensor permutation. The impedance and phase delay profiles of the aortas varied in accordance with the degree of plaque development. Within the "plateau region" of 40 Hz to 40 kHz (dashed rectangles)—the frequency range throughout which impedance values are stable, thus allowing for accurate comparisons between measurements—initiating plaques (blue) exhibited (E) a lower impedance, and (F) a phase delay profile that peaked at a higher frequency compared to progressing plaques (red). EIS, electrochemical impedance spectroscopy.
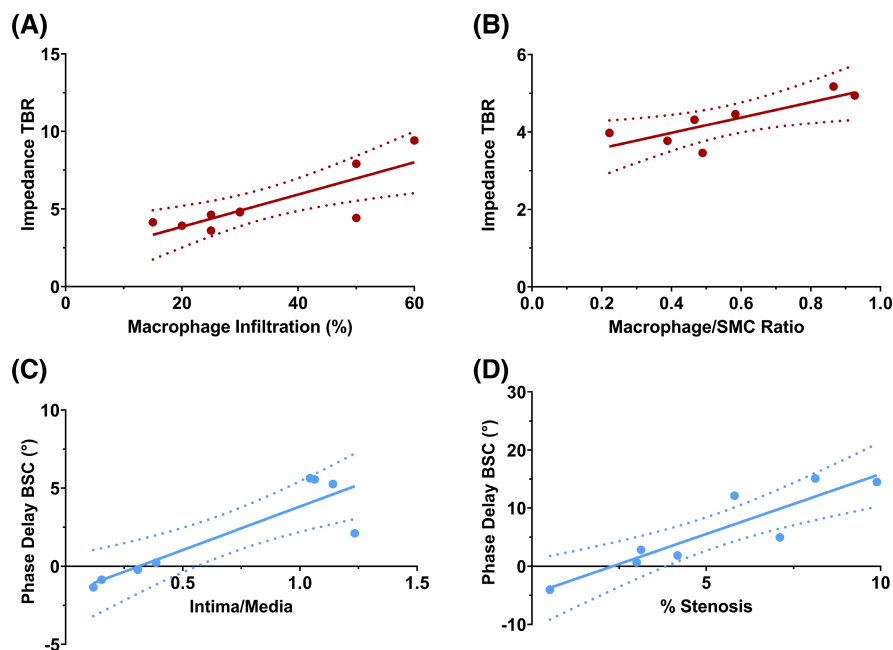

FIGURE 5 Detection of plaque composition and morphology by EIS. The impedance and phase delay profiles of rabbit abdominal aortas were measured via EIS in vivo. (A and B) Impedance TBR correlated significantly with macrophage infiltration ($r = .813$, $p = .008$) and macrophage/SMC ratio ($r = .813$, $p = .026$). (C and D) Phase delay BSC demonstrated significant correlation with intima/media ratio ($r = .883$, $p = .004$) and %stenosis ($r = .901$, $p = .002$). Pearson correlation coefficients were calculated for comparison of EIS impedance and phase delay against histological parameters. BSC, background subtraction correction; EIS, electrochemical impedance spectroscopy. SMC, smooth muscle cell. TBR, target-to-background ratio.
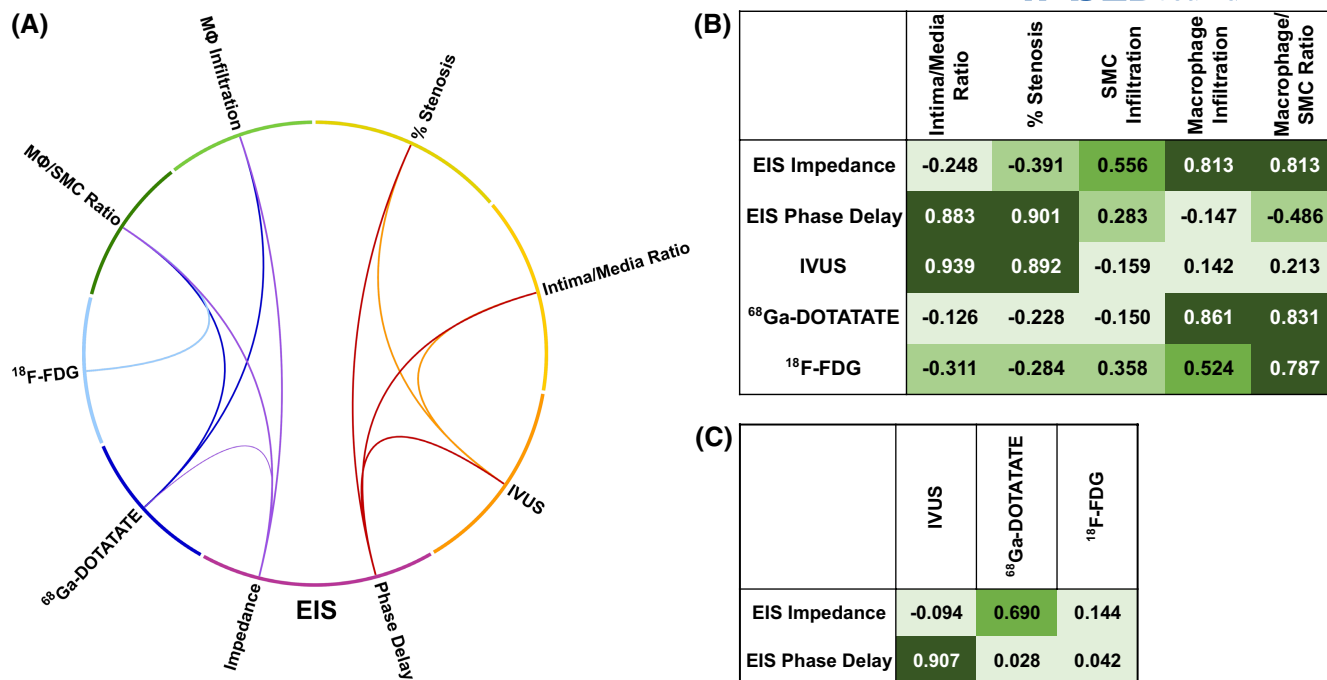
(A)

(B)

	Intima/Media Ratio	% Stenosis	SMC Infiltration	Macrophage Infiltration	Macrophage/SMC Ratio
EIS Impedance	-0.248	-0.391	0.556	0.813	0.813
EIS Phase Delay	0.883	0.901	0.283	-0.147	-0.486
IVUS	0.939	0.892	-0.159	0.142	0.213
68Ga-DOTATATE	-0.126	-0.228	-0.150	0.861	0.831
18F-FDG	-0.311	-0.284	0.358	0.524	0.787

(C)

	IVUS	68Ga-DOTATATE	18F-FDG
EIS Impedance	-0.094	0.690	0.144
EIS Phase Delay	0.907	0.028	0.042

FIGURE 6 Correlation of EIS, PET, IVUS, and histological plaque parameters. (A) The thickness of each curve represents the magnitude of correlation, with numerically greater correlations depicted by thicker curves. Only statistically significant correlations are shown. (B) Correlation of imaging modalities with plaque parameters assessed by histology. (C) Correlation of EIS impedance and phase delay with IVUS and PET measures of atherosclerosis. Correlation strengths are sorted into the following categories: 0.00–0.25, 0.26–0.50, 0.51–0.75, and 0.76–0.99, with corresponding color. Statistically significant correlations are underlined. EIS, electrochemical impedance spectroscopy; 18F-FDG, 18F-fluorodeoxyglucose; 68Ga-DOTATATE, 68Ga-tetraazacyclododecanetetraacetic acid-DPhe1-Tyr3-octreotate; IVUS, intravascular ultrasound; MΦ, macrophage; SMC, smooth muscle cell.

indicate (iii) enhanced EIS signal specificity when conducting background correction measures, and (iv) signal stability between various EIS sensors.

Initial studies in animal models demonstrated EIS discernment of atherosclerotic from healthy tissue via frequency-dependent electrical impedance.[14,15,17] However, the focal nature of the catheter designs utilized in these studies inadequately captures the heterogeneity of atherosclerosis; these sensors would need to be rotated between measurements to account for plaque eccentricity. Catheter rotation while under balloon inflation carries the risk of iatrogenic plaque disruption or vessel wall injury. Conversely, deflating the balloon prior to rotation might shift the placement of the sensors, thus affecting the accuracy of atherosclerotic assessment at that vessel segment. The 6-point, circumferential design utilized in the present study allows for uninterrupted 360° interrogation of a vessel segment. Furthermore, the 15 unique measurement permutations begotten by the 6-point design, combined with the reduced electrode dimensions, improve spatial resolution by facilitating more granular measurement of a vessel segment.

Intravascular strategies such as imaging or stent deployment may induce endothelial injury, thus increasing potential thrombotic complications. The size and

flexibility of intravascular devices may influence the degree of vascular injury following deployment. For example, intravascular imaging catheters and guidewires are flexible and generally of small dimensions, thereby reducing injury risk.[18] Our EIS catheter has an external diameter appr. equivalent to a 3F catheter and possesses potential to be further miniaturized. Thus, while EIS interrogation may precipitate endothelial injury, we do not anticipate major complications.

To assess the in vivo detection by 3-D EIS signals of atherosclerotic processes of interest, we first evaluated specific plaque components by relevant PET radiotracers studied extensively in both preclinical and clinical investigations. Plaque macrophage content, and more particularly an increased macrophage/SMC ratio, is a known histological indicator of downstream atherosclerotic complications.[2,3] 18F-FDG did not correlate with macrophage infiltration alone and only moderately with the macrophage/SMC ratio. 18F-FDG lacks specificity as any cell type that utilizes glucose for metabolism, such as cardiomyocytes, will uptake 18F-FDG, leading to limited signal specificity and significant background noise. Previous research indicated a lack of correlation between 18F-FDG uptake and CD68 macrophage staining[19] and unfavorable cardiovascular disease risk profiles.[20] To

address the issue of non-specificity, ^{68}Ga-DOTATATE was developed as a somatostatin receptor 2 (SSTR2) agonist. Given that proinflammatory macrophages express SSTR2, ^{68}Ga-DOTATATE has higher specificity to image plaque macrophages.[21] In the present study, ^{68}Ga-DOTATATE correlated strongly with both macrophage infiltration and the macrophage/SMC ratio. ^{18}F-NaF has emerged as a powerful non-invasive method to determine atherosclerotic lesion activity via PET. We observed a significant, strong correlation between ^{18}F-NaF uptake and calcified area. Mechanistically, the ^{18}F-fluoride ion exchanges with a hydroxyl group in hydroxyapatite crystals; consequently, ^{18}F-NaF is capable of visualizing plaque microcalcification, itself correlated with lesion expansion and thus plaques that are deemed "unstable." Despite our results supporting ^{18}F-NaF detection of microcalcification, this was present in $n = 3$ rabbits only, limiting our ability to assess EIS detection of microcalcification. We also observed a strong negative correlation between ^{18}F-NaF and SMC infiltration into the intima, likely due to their known transdifferentiation into an osteochondrogenic-like cell type that contributes to vascular calcification.[22–26]

PET imaging, despite its versatility and clinical applicability, suffers from certain drawbacks, primarily its limited spatial resolution and reliance on radiotracers. The spatial resolution of PET (0.5–2 mm for μPET and 4–5 mm for clinical PET)[27,28] is orders of magnitude worse than those of intravascular imaging modalities (100–200 μm for IVUS and NIRF and 10–20 μm for OCT).[29,30] Furthermore, accurate PET imaging relies on the radiotracer localizing with the target of interest and minimal background uptake.[9] An increasingly utilized alternative to invasive coronary angiography (ICA) is coronary CTA,[31,32] which may be paired with fractional flow reserve by computed tomography (FFR-CT),[33] allowing improvement in its specificity[4] and the serial assessment of CAD burden.[34,35] However, CTA exposes patients to ionizing radiation, suffers from blooming artifacts, and is dependent on iodinated contrast agents. Magnetic resonance imaging (MRI) boasts excellent soft tissue contrast and plaque component discrimination,[2,36,37] but remains an expensive strategy and is more suited for larger, "immobile" arteries such as the carotids given its sensitivity to cardiac and respiratory motion.

IVUS provides morphological assessment of vessel lesions, such as vessel wall dimensions and luminal narrowing. However, IVUS suffers from low spatial resolution and a limited ability to distinguish plaque components.[10] Recently, IVUS has been paired with complementary imaging modalities that shore up its shortcomings, such as OCT, near-infrared spectroscopy (NIRS), or NIRF. OCT provides excellent spatial resolution but lacks penetration depth.[11,12] NIRS reliably produces semiquantitative information on plaque lipid content, but is of limited utility otherwise. NIRF captures in vivo pathobiological processes and visualizes pertinent biological activity at the plaque and cellular level.[10,38,39] Due to the nature of NIRF, it is entirely dependent on the administration of targeting probes and thus vulnerable to the limitations inherent to a probe and its biodistribution that may reduce plaque TBR.[10,38]

The present study establishes EIS detection of important atherosclerosis compositional features. EIS impedance demonstrates strong, positive correlation with both macrophage content and macrophage/SMC ratio. SMC secretion of collagen and elastin provides mechanical stability to the fibrous cap and maintains a barrier between the thrombogenic core and circulating coagulation factors.[40] Conversely, macrophages release proteases such as matrix metalloproteinases that degrade collagen and decrease the plaque's mechanical stability. Plaque macrophage density inversely correlates with fibrous cap integrity.[41] Consequently, risk of plaque rupture grows with increasing macrophage/SMC ratio.[42] These key features are detected by changes in EIS impedance profiles.

EIS also elucidates morphological features of atherosclerotic plaque via phase delay. Culprit lesion analysis of patients with coronary complications revealed luminal narrowing of 50% to 75% as an optimal threshold to identify rupture-prone lesions.[43,44] Our results demonstrate a strong correlation between EIS phase delay and both %stenosis and intima/media ratio. However, we emphasize that the main proposed use of EIS in CAD evaluation is detection of metabolically active, rupture-prone atherosclerotic lesions, not the assessment of stenosis severity for which several excellent modalities are used routinely. There may be cases in which visual analysis is inaccurate in estimating luminal narrowing; we posit that EIS phase delay identification of severe stenoses may serve as an additive strategy to ICA.

We propose EIS may serve as a complementary modality to ICA. Under fluoroscopy, EIS sensors may be apposed to a coronary segment of interest for plaque interrogation. EIS impedance profiles would permit identification of atherosclerotic lesions with significant macrophage accumulation and high macrophage-to-vascular SMC ratio — high-risk plaque features portending rupture risk. In the present experimental study, we demonstrate the ability of 3-D EIS to unravel key atherosclerotic features that would otherwise require multiple PET radiotracers and complementary IVUS for identification. Future research will need to determine whether EIS can serve to guide changes in medical therapy and/or preemptive coronary revascularization.

Our study has limitations. Although there are various methods for quantifying macrophage content (e.g.,

counting nuclei), we opted for visual evaluation rather than specific staining due to the absence of commercially available anti-rabbit antibody products that reliably stain macrophages in rabbit tissues. Despite trying two different antibody products targeting CD68, one targeting CD204 and one targeting PU.1, none of these yielded satisfactory staining suitable for quantification. Furthermore, the atherosclerotic lesions were experimentally induced and thus are not necessarily representative of human lesions. Additionally, EIS was measured at one time point (immediately prior to animal euthanasia). Future research should assess the ability of serial EIS-derived measures to scrutinize structural and compositional changes that may occur in atherosclerosis. Furthermore, we posit that our results lay the foundation for invasive EIS interrogation of human coronary atherosclerotic lesions and the determination of clinically relevant threshold values for impedance and phase delay that may help guide coronary revascularization decision-making.

5 | CONCLUSIONS

EIS distinguishes inflammatorily active from quiescent lesions by detecting key atherosclerosis features that otherwise require multiple imaging modalities to capture. Thus, EIS may be a valuable tool for comprehensive CAD evaluation given its ability to characterize both plaque anatomy and underlying activity.

ORCID
Michael Chen https://orcid.org/0000-0003-0694-6641
Shili Xu https://orcid.org/0000-0002-4933-8673
Krit Suwannaphoom https://orcid.org/0009-0009-6036-829X
Gentian Lluri https://orcid.org/0000-0002-4000-8993
Mikayla Tamboline https://orcid.org/0000-0002-3675-2904
Sandra Duarte https://orcid.org/0009-0004-7671-2589
Michael C. Fishbein https://orcid.org/0000-0002-6591-6306
Yuan Luo https://orcid.org/0000-0003-3153-7495
René R. Sevag Packard https://orcid.org/0000-0002-8520-5843

REFERENCES
1. Martin SS, Aday AW, Almarzooq ZI, et al. 2024 heart disease and stroke statistics: a report of US and global data from the American Heart Association. *Circulation*. 2024;149:e347-e913.
2. Gaba P, Gersh BJ, Muller J, Narula J, Stone GW. Evolving concepts of the vulnerable atherosclerotic plaque and the vulnerable patient: implications for patient care and future research. *Nat Rev Cardiol*. 2023;20:181-196.
3. Libby P, Pasterkamp G, Crea F, Jang I-K. Reassessing the mechanisms of acute coronary syndromes: the "vulnerable plaque" and superficial erosion. *Circ Res*. 2019;124:150-160.
4. Packard RRS, Li D, Budoff MJ, Karlsberg RP. Fractional flow reserve by computerized tomography and subsequent coronary revascularization. *Eur Heart J Cardiovasc Imaging*. 2017;18:145-152.
5. Packard RRS, Votaw JR, Cooke CD, Van Train KF, Garcia EV, Maddahi J. ^{18}F-flurpiridaz positron emission tomography segmental and territory myocardial blood flow metrics: incremental value beyond perfusion for coronary artery disease categorization. *Eur Heart J Cardiovasc Imaging*. 2022;23:1636-1644.
6. Rominger A, Saam T, Vogl E, et al. In vivo imaging of macrophage activity in the coronary arteries using ^{68}Ga-DOTATATE PET/CT: correlation with coronary calcium burden and risk factors. *J Nucl Med*. 2010;51:193-197.
7. Joshi NV, Vesey AT, Williams MC, et al. ^{18}F-fluoride positron emission tomography for identification of ruptured and high-risk coronary atherosclerotic plaques: a prospective clinical trial. *Lancet*. 2014;383:705-713.

8. Tawakol A, Migrino RQ, Bashian GG, et al. In vivo ^{18}F-fluorodeoxyglucose positron emission tomography imaging provides a noninvasive measure of carotid plaque inflammation in patients. *J Am Coll Cardiol*. 2006;48:1818-1824.

9. Sadeghi MM, Glover DK, Lanza GM, Fayad ZA, Johnson LL. Imaging atherosclerosis and vulnerable plaque. *J Nucl Med*. 2010;51:51S-65S.

10. Khraishah H, Jaffer FA. Intravascular molecular imaging: near-infrared fluorescence as a new frontier. *Front Cardiovasc Med*. 2020;7:587100. doi:10.3389/fcvm.2020.587100

11. Milzi A, Lemma ED, Dettori R, et al. Coronary plaque composition influences biomechanical stress and predicts plaque rupture in a morpho-mechanic OCT analysis. *Elife* 2021;10:e64020.

12. Araki M, Park S-J, Dauerman HL, et al. Optical coherence tomography in coronary atherosclerosis assessment and intervention. *Nat Rev Cardiol*. 2022;19:684-703.

13. Khraishah H, Jaffer FA. Intravascular molecular imaging to detect high-risk vulnerable plaques: current knowledge and future perspectives. *Curr Cardiovasc Imaging Rep*. 2020;13:8.

14. Süselbeck T, Thielecke H, Köchlin J, et al. Intravascular electric impedance spectroscopy of atherosclerotic lesions using a new impedance catheter system. *Basic Res Cardiol*. 2005;100:446-452.

15. Packard RRS, Zhang X, Luo Y, et al. Two-point stretchable electrode Array for Endoluminal electrochemical impedance spectroscopy measurements of lipid-laden atherosclerotic plaques. *Ann Biomed Eng*. 2016;44:2695-2706.

16. Packard RRS, Luo Y, Abiri P, et al. 3-D electrochemical impedance spectroscopy mapping of arteries to detect metabolically active but angiographically invisible atherosclerotic lesions. *Theranostics*. 2017;7:2431-2442.

17. Yu F, Li R, Ai L, et al. Electrochemical impedance spectroscopy to assess vascular oxidative stress. *Ann Biomed Eng*. 2011;39:287-296.

18. Autar A, Taha A, Van DR, et al. Endovascular procedures cause transient endothelial injury but do not disrupt mature neointima in drug eluting stents. *Sci Rep*. 2020;10:2173.

19. Myers KS, Rudd JHF, Hailman EP, et al. Correlation between arterial FDG uptake and biomarkers in peripheral artery disease. *JACC Cardiovasc Imaging*. 2012;5:38-45.

20. Blomberg BA, De JPA, Thomassen A, et al. Thoracic aorta calcification but not inflammation is associated with increased cardiovascular disease risk: results of the CAMONA study. *Eur J Nucl Med Mol Imaging*. 2017;44:249-258.

21. Tarkin JM, Joshi FR, Evans NR, et al. Detection of atherosclerotic inflammation by ^{68}Ga-DOTATATE PET compared to [^{18}F] FDG PET imaging. *J Am Coll Cardiol*. 2017;69:1774-1791.

22. Tintut Y, Honda HM, Demer LL. Biomolecules orchestrating cardiovascular calcification. *Biomolecules*. 2021;11:1482.

23. Voelkl J, Lang F, Eckardt K-U, et al. Signaling pathways involved in vascular smooth muscle cell calcification during hyperphosphatemia. *Cell Mol Life Sci*. 2019;76:2077-2091.

24. Durham AL, Speer MY, Scatena M, Giachelli CM, Shanahan CM. Role of smooth muscle cells in vascular calcification: implications in atherosclerosis and arterial stiffness. *Cardiovasc Res*. 2018;114:590-600.

25. Speer MY, Yang H-Y, Brabb T, et al. Smooth muscle cells give rise to osteochondrogenic precursors and chondrocytes in calcifying arteries. *Circ Res*. 2009;104:733-741.

26. Naik V, Leaf EM, Hu JH, et al. Sources of cells that contribute to atherosclerotic intimal calcification: an in vivo genetic fate mapping study. *Cardiovasc Res*. 2012;94:545-554.

27. Lai Y, Wang Q, Zhou S, et al. H2RSPET: a 0.5 mm resolution high-sensitivity small-animal PET scanner, a simulation study. *Phys Med Biol*. 2021;66:065016.

28. Moghbel M, Al-Zaghal A, Werner TJ, Constantinescu CM, Høilund-Carlsen PF, Alavi A. The role of PET in evaluating atherosclerosis: a critical review. *Semin Nucl Med*. 2018;48:488-497.

29. Truesdell AG, Alasnag MA, Kaul P, et al. Intravascular imaging during percutaneous coronary intervention. *J Am Coll Cardiol*. 2023;81:590-605.

30. Yoo H, Kim JW, Shishkov M, et al. Intra-arterial catheter for simultaneous microstructural and molecular imaging in vivo. *Nat Med*. 2011;17:1680-1684.

31. Blankstein R, Shaw LJ, Gulati M, et al. Implications of the 2021 AHA/ACC/ASE/CHEST/SAEM/SCCT/SCMR CHEST pain guideline for cardiovascular imaging: a multisociety viewpoint. *JACC Cardiovasc Imaging*. 2022;15:912-926.

32. Park H-B, Heo R, Hartaigh BÓ, et al. Atherosclerotic plaque characteristics by CT angiography identify coronary lesions that cause ischemia. *JACC Cardiovasc Imaging*. 2015;8:1-10.

33. Dodd JD, Leipsic JA. Evolving developments in cardiac CT. *Radiology*. 2023;307:e222827.

34. Rabbat MG, Lakshmanan S, Benjamin MM, et al. Benefit of icosapent ethyl on coronary physiology assessed by computed tomography angiography fractional flow reserve: EVAPORATE-FFRCT. *Eur Heart J Cardiovasc Imaging*. 2023;24:866-873.

35. Chen M, Almeida SO, Sayre JW, Karlsberg RP, Packard RRS. Distal-vessel fractional flow reserve by computed tomography to monitor epicardial coronary artery disease. *Eur Heart J Cardiovasc Imaging*. 2024;25:163-172.

36. Fleg JL, Stone GW, Fayad ZA, et al. Detection of high-risk atherosclerotic plaque. *JACC Cardiovasc Imaging*. 2012;5:941-955.

37. Kerwin WS, O'Brien KD, Ferguson MS, Polissar N, Hatsukami TS, Yuan C. Inflammation in carotid atherosclerotic plaque: a dynamic contrast-enhanced MR imaging study. *Radiology*. 2006;241:459-468.

38. Khamis RY, Woollard KJ, Hyde GD, et al. Near infrared fluorescence (NIRF) molecular imaging of oxidized LDL with an autoantibody in experimental atherosclerosis. *Sci Rep*. 2016;6:21785.

39. Hara T, Bhayana B, Thompson B, et al. Molecular imaging of fibrin deposition in deep vein thrombosis using fibrin-targeted near-infrared fluorescence. *JACC Cardiovasc Imaging*. 2012;5:607-615.

40. Bentzon JF, Otsuka F, Virmani R, Falk E. Mechanisms of plaque formation and rupture. *Circ Res*. 2014;114:1852-1866.

41. Lendon CL, Davies MJ, Born GVR, Richardson PD. Atherosclerotic plaque caps are locally weakened when macrophages density is increased. *Atherosclerosis*. 1991;87:87-90.

42. Newby AC, Zaltsman AB. Fibrous cap formation or destruction — the critical importance of vascular smooth muscle cell proliferation, migration and matrix formation. *Cardiovasc Res*. 1999;41:345-360.

43. Virmani R, Burke AP, Farb A, Kolodgie FD. Pathology of the vulnerable plaque. *J Am Coll Cardiol*. 2006;47:C13-C18.

44. Narula J, Nakano M, Virmani R, et al. Histopathologic characteristics of atherosclerotic coronary disease and implications

of the findings for the invasive and noninvasive detection of vulnerable plaques. *J Am Coll Cardiol.* 2013;61:1041-1051.

SUPPORTING INFORMATION

Additional supporting information can be found online in the Supporting Information section at the end of this article.